Nanoparticle Biokinetics in Mice and Nonhuman Primates

Peter A. Chiarelli[†,&], **Richard A. Revia**[†,&], **Zachary R. Stephen**[†,&], **Kui Wang**[‡], **Mike Jeon**[‡], **Veronica Nelson**[§], **Forrest M. Kievit**[†,‡], **Jonathan Sham**[#], **Richard G. Ellenbogen**[†,▽], **Hans-Peter Kiem**[§,⊥], and **Miqin Zhang**[†,‡,▽,*]

[†]Department of Neurological Surgery, University of Washington, Seattle, Washington 98195

[‡]Department of Materials Science and Engineering, University of Washington, Seattle, Washington 98195

[§]Clinical Research Division, Fred Hutchinson Cancer Research Center, Seattle, WA 98109, USA

[#]Department of Surgery, University of Washington, Seattle, Washington 98195

[▽]Department of Radiology, University of Washington, Seattle, Washington 98195

[⊥]Department of Medicine and Pathology, University of Washington, Seattle, WA, USA

Abstract

Despite the preponderance of iron oxide nanoparticles (NPs) designed for theranostic applications, widespread clinical translation of these NPs lags behind. A better understanding of how NP pharmacokinetics vary between small and large animal models is needed to rapidly customize NPs for optimal performance in humans. Here we use noninvasive magnetic resonance imaging (MRI) to track iron oxide NPs through a large number of organ systems *in vivo* to investigate NP biokinetics in both mice and nonhuman primates. We demonstrate that pharmacokinetics are similar between mice and macaques in the blood, liver, spleen, and muscle, but differ in the kidneys, brain, and bone marrow. Our study also demonstrates that full-body MRI is practical, rapid and cost-effective for tracking NPs non-invasively with high spatiotemporal resolution. Our techniques using a nonhuman primate model may provide a platform for testing a range of NP formulations.

Graphical Abstract

[*]Corresponding Author: Miqin Zhang, Department of Materials Science & Engineering, University of Washington, mzhang@uw.edu, 302L Roberts Hall, Box 352120, Seattle, WA 98195, Fax: (206) 543-3100.
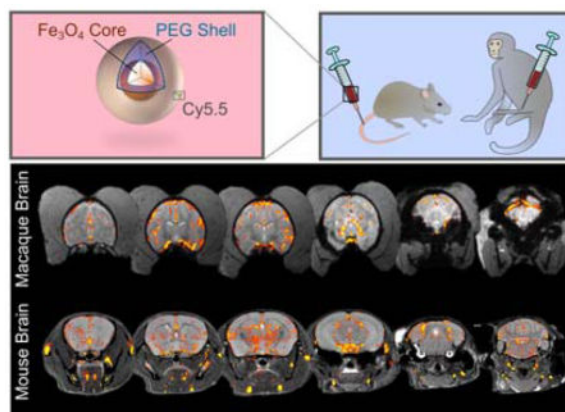[&]**Author Contributions**
These authors contributed equally to this publication

Conflict of Interest
The authors declare no competing financial interest.

Keywords

iron oxide nanoparticle; biokinetics; cross-species; magnetic resonance imaging; nonhuman primates; mice

Nanostructured materials have the potential to transform the diagnosis and treatment of many diseases, including neoplasms.[1] Although the number of successful pre-clinical nanoparticle (NP) studies is rapidly growing, NPs have been relatively slow to reach the clinic,[2] and only a very few low-toxicity NP formulations have entered clinical trials.[3–4] A shared opinion in the field is the need to more fully understand how experimental NPs might distribute throughout the human body.[5–7] Such knowledge would help predict treatment effects, as well as toxicity in organs of excretion and the hematopoietic bone marrow compartment.[2,8]

It has been well-established in rodent models that NP size, charge, and surface coatings greatly influence biodistribution.[9–11] Murine NP biokinetics has been investigated *via* magnetic resonance imaging (MRI),[12–13] radioactive labeling,[14–15] inductively coupled plasma (ICP) measurement,[16–17] and visible light imaging.[10] MRI, specifically, can be repeated *in vivo* without ionizing radiation, and murine studies have used MRI to non-invasively monitor NPs as they traverse 3–4 organs over time.[9,13,18–20] A study seems overdue that demonstrates the *in vivo* MR tracking of particles through all major organ systems, while translating this knowledge of NP biodistribution from the common lab mouse to a species more physiologically comparable to humans. Without direct experiments, the assumption of equivalent biokinetics between mice and primates is a risky one, and it can lead to under-informed clinical trials requiring cessation from unexpected toxicity and off-target delivery.

In this work, we report on the inter-species comparison of NP biokinetics between mice and nonhuman primates (NHPs) and provide a systematic study that continuously tracks NPs in macaques using MRI through the largest number of organ systems accomplished to date. NHPs are preferred animals for pre-clinical identification of NP biokinetics and toxicity profile as NHPs approximate humans in physiology and genetics more closely than any other animal.[21] MRI is a convenient tool to quickly and non-invasively test NP biokinetics in

NHPs where the number of NHPs is limited and radiation quantification is not feasible or accessible. We compare *in vivo* organ uptake of an iron oxide NP coated with a siloxane poly(ethylene glycol) (PEG) monolayer (IOSPM) between the two species. The IOSPM has a number of favorable properties as a contrast agent for clinical use including superparamagnetic property, small and uniform size, high stability in aqueous solutions, and excellent biodegradability.[22] We find that NP kinetics are nearly identical in blood, liver, spleen, and muscle but differ in brain, bone marrow, and kidney between the two species. Our approach allows us to resolve and quantify MRI signal with temporal and spatial resolutions not obtainable by other existing non-invasive imaging modalities. The work here describes IOSPM NP organ kinetics providing valuable physiological information and presents a cost-effective, widely applicable strategy to assist in the clinical translation of NPs.

RESULTS AND DISCUSSION

Characterization of the nanoparticle system

IOSPM NP (Figure 1a) were designed to maximize MRI contrast and provide comparable chemical behavior to iron oxide NPs commonly used in the literature. Oleic acid coated iron oxide NPs (IOOAs) were synthesized by thermal decomposition of iron organometallic compounds, yielding monodisperse nanoparticles.[23] Silanization and subsequent grafting of amine-functionalized PEG displaced oleic acid from the IOOA surface, thereby enhancing water solubility.[24]

Superparamagnetic iron oxide nanoparticle (SPION) core size has a significant effect on MR relaxivity, and impacts MRI contrast *in vivo*.[25] IOSPM NPs had a core size of 12 nm, determined by TEM (Figure 1b). R2 (1/T2) relaxivities of the NPs in phosphate buffered saline (PBS) were evaluated to be 45.3 and 61.4 s^{-1} mM^{-1}, at 3 T and 14 T field strengths, respectively (Figure 1c). A linear relationship was established between quantitative T2 measurements and relative changes in T2*- weighted signal, as particle concentration varied (Figure 1d).

Hydrodynamic size and surface properties of NPs are primary factors that dictate *in vivo* uptake, retention, and clearance.[10,26] The IOSPM NP hydrodynamic diameter was 31.5 ± 2.0 nm in PBS (Figure 1e), well within the range to minimize renal and mononuclear phagocyte system clearance[26]. IOSPM NPs remained stable in biologically relevant fluid, Dulbecco's Modified Eagle's Medium (DMEM) with 10% fetal bovine serum (FBS), over 10 days (Figure 1f). At pH 7.4, IOSPM NPs had a modestly negative zeta-potential of −14.4 ± 7.2 mV (Figure 1g).

A subset of IOSPM NPs was labeled with Cy5.5, a near-infrared fluorophore, to facilitate whole-organ fluorescence imaging. UV-vis spectroscopy was utilized to quantitate Cy5.5 labeling (Figure 1h). Based on the absorbance maximum (673 nm) of IOSPM-Cy5.5 and the extinction coefficient of Cy5.5 (2.09×10^5 $M^{-1}cm^{-1}$), the molar ratio of fluorophore:IOSPM was calculated to be 50:1.

In vivo NP tracking in macaque organs

IOSPM NPs were delivered to three macaques by saphenous vein injection. As our pilot experiments show full clearance of clinically-relevant low-dose IOSPM NPs (2.4 mg Fe/kg) from the blood within 4 hours, we scanned animals during this timeframe using interleaved quantitative T2 (QT2), quantitative T2* (QT2*), and T2*-weighted (T2*-W) imaging. MR monitoring of the head and full torso was performed using T2 mapping up to 4 h after injection (Figure 2). Figure 2a displays a T2 map of the liver before and after NP injection, with relatively consistent NP uptake (red) across the organ. A rapid change in liver T2 from 45 to 24 ms occurred after injection, indicative of expected first-pass metabolism. Sagittal (Figure 2b) and coronal (Figure 2c) views are provided of the upper torso, with colored regions of interest (ROIs) marked. Raw data from a multi-spin echo QT2 sequence (Figure 2d) demonstrates good signal in liver (red dashed line), spleen (green dashed line), and kidney (purple dashed line). An inset shows a separate slice of the kidney, with renal pelvis highlighted (orange).

Color-coded ROIs were used to interrogate QT2 images, with temporal T2 plots obtained from 8 compartments: blood (yellow), muscle (grey), renal cortex (purple), renal pelvis (orange), spleen (green), marrow (light blue), deep grey matter (dark blue), and liver (red) (Figure 2e). T2 values at $t = 0$ were acquired immediately before NP injection. Inspection of the carotid artery lumen demonstrates an immediate post-injection change in T2, followed by elimination with a linear decay profile ($R^2 = 0.97$). From a pharmacological perspective, linear (zero-order) kinetics suggests that the elimination biomachinery of NP is saturated. The half-life of the IOSPM NP is ~2 h.

Time courses from the three macaques demonstrate considerable similarity between animals. In muscle, there is little T2 change after NP injection, suggesting a negligible amount of NPs present in muscle. In liver and spleen, T2 changes rapidly and saturates for the duration of imaging, suggesting that NPs remain in the liver and spleen at 4 h. The renal cortex of three animals shows comparable profiles of NP uptake followed by elimination. MRI behavior in renal cortex is accompanied by information from the renal pelvis, the space where new urine is first expelled as it travels to the bladder. Prior to NP injection, the T2 of urine in the renal pelvis closely matches the T2 of water at 3 T (~250 ms). The T2 in the renal pelvis falls after injection, and plateaus around the same time (~2 h) when the renal cortex time course reaches its minimum. In the marrow and brain, T2 slowly decreases and reaches a minimum value between 1–3 h after injection. The temporal window of 4 h captures the beginning of NP elimination from marrow and brain, although a full return to baseline is incompletely visualized.

Within each organ, changes in T2 arise from a combination of intravascular and extravascular NPs. Relative blood volume can therefore be expected to influence measured T2 behavior. Although large vessels were avoided when placing the ROIs, there is no way to eliminate vascular partial volume effects. We are reassured by the disparate trends between carotid blood T2 and the T2 of other organs, suggesting that the vascular influence on organ T2 is minimal. Muscle is a compartment with high vascularity, yet demonstrates negligible change. Splenic and hepatic T2 remain at a plateau even as blood T2 returns to baseline. Brain and marrow display significantly delayed NP uptake compared to the blood time

course, and renal kinetics are entirely different from the signal profile in blood. Another biophysical influence that may alter T2 and T2* is the bulk magnetic susceptibility change that occurs when NPs form intracellular clusters, leading to a breakdown of quantum mechanical static dephasing assumptions.[27–29] This effect is explored in Supporting Information (Supporting Information Figure 1).

In vivo NP biokinetics in mice

Mice were injected using the same dose (2.4 mg Fe/kg), MR scanning duration (4 h), and same IOSPM NP synthetic batch as the macaques. We selected the nude athymic mouse, a common choice practiced in most laboratories, to provide the greatest relevance to studies of contrast agents. Transverse cross-sections of mouse anatomy from pelvis to head acquired by high-resolution 14 T MRI are shown in Figure 3a. 14 T MRI delivered greater MR sensitivity to the NP than 3 T, while maintaining necessary linearity between NP concentration and T2 or T2* (Figures 1c, d). Representative raw images are provided in Supporting Information (Supporting Information Figure 2). IOSPM NP uptake and elimination are shown in Figure 3, based on T2*-W signal change (Figure 3b) and QT2 (Figure 3c), indicating that the half-life of the IOSPM NP is ~2 h. Multi-animal averages are shown as colored lines, while data from individual animals are shown in grey. Excellent overall correspondence is seen between animals.

The use of interleaved T2*-W and QT2 acquisition provided high-quality data in a large number of organ compartments. With shorter overall T2 values at 14 T compared to 3 T, automated QT2 calculation was potentially prone to occasional inaccurate fitting of decay curves, especially in areas such as the liver and blood with T2   20 ms. We therefore performed manual non-linear curve fitting for calculation of all T2 values, and have displayed representative fits in Supporting Information (Supporting Information Figure 3). The spleen posed a different challenge for QT2 imaging, as the bright and dark speckled architecture generated artifact from slight respiratory motion between spin-echoes. We relied solely on T2*-W data in the spleen because of these artifacts (described in Supporting Information, Supporting Information Figure 4). QT2 data was exclusively used in the liver, as high baseline iron content made the quickly decaying T2*-W signal nearly black, even prior to NP injection. The subtle T2*-W signal change in the brain was detectable with the high contrast-to-noise properties of T2*-W imaging, but not with QT2 brain imaging (Supporting Information, Supporting Information Figure 5). MRI was not used to interrogate the lung or heart, due to lung air spaces and cardiac motion. All T2*-W trends include linear correction of baseline signal by the intensity of an adjacent water phantom, to account for fluctuations in hardware sensitivity (Supporting Information, Supporting Information Figure 6).

To support MRI-derived trends, we performed near-infrared fluorescence (NIRF) imaging of extracted organs, after injection of fluorescently-labeled IOSPM NPs (Figure. 4). Prior validation of this *ex vivo* method showed comparable results from whole organs and histological sections.[30–31] 4 groups of nude mice were used, with one group receiving no injection, and mice of the other groups sacrificed at sequential times after injection. While the addition of a fluorescent label may somewhat alter the surface properties of the NPs, key

characteristics including hydrophilic coating (PEG), core size (12 nm), hydrodynamic size (27.7 nm), and zeta-potential (−12.1 mV) were similar to the non-labeled NPs.

Figure 4a displays NIRF organ images, along with 200 μl of whole blood from each mouse. NP accumulation was greatest in liver, with substantial relative quantities found in blood, bone, kidney, and spleen. NIRF timecourses are displayed in Figure 4b and agree qualitatively with MRI trends. Plotting matched MRI and NIRF data, we observed a linear correlation (R^2 = 0.93–0.96) (Figure 4c). Representative QT2 comparisons with NIRF are shown for renal cortex and liver, and T2*-W comparison data with NIRF is shown for marrow and brain.

Inter-species biokinetics are organ-dependent

T2*-W changes are displayed within the mouse and macaque brain, 30 min after NP injection (Figure 5a). These scans show predominant intravascular NP effects (color threshold = 10 % signal change). From an examination of Figures 2 and 3, we know that signal changes occur in areas of the deep grey matter chosen to avoid large vessels. These signal changes are smaller (~6 %), delayed in peak uptake and elimination compared to blood signal, and highly reproducible between animals. The signal profile in large vessels (*e.g.*, sagittal sinus, white dashed line) achieves an immediate peak and displays zero-order elimination kinetics, similar to behavior of the carotid.

Figure 5b shows a direct comparison of macaque and mouse biokinetics, with mouse data sub-sampled at equivalent timepoints to macaque data and trends scaled so that minimum and maximum values in either species were re-calibrated to values of 0 and 100, respectively. Using these amplitude-matched curves, the relative difference between macaque and mouse was calculated. In the renal pelvis at 1 h, the mouse displayed ~2× greater signal change compared to the macaque, and −50 % is displayed on the comparison plot; at 3 h, the mouse trend shows nearly complete washout, while the macaque trend was at its peak, and therefore, a large positive difference (+80%) is displayed. Despite dissimilar kinetics in the kidney and prolonged elimination from macaque brain and marrow, IOSPM NP kinetics are similar in blood, liver, spleen, and muscle. MR profiles in the blood are further supported by highly linear correlation with macaque plasma iron measurement (Figure 5c) and mouse blood fluorescence measurement (Figure 5d). Plasma iron data show a 9 μg/ml variation over the 3.5 h period of MR data collection. Zero-order iron elimination from the macaque occurs at a rate of 2.6 μg/ml/hr, corresponding to a T2 reduction of 7.3 ms/hr.

Nanoparticle acute toxicity evaluation in Macaque

Macaque clinical laboratory data is shown in Figure 6. Prior work demonstrated lack of murine toxicity for a similar NP base formulation.[30]. Inspection of macaque cell count (Figure 6a) reveals no elevation outside of reference ranges in white blood cells (WBC; reference range in macaque= 8.1–15.4), which would otherwise indicate an immune response. However, the percentage of neutrophils showed a minimal, transient increase at 4 h post injection but returned to baseline by 2 weeks indicating possible mild, acute stress. Considering the prolonged retention of IOSPM NPs in the macaque bone marrow, it is

important to see no evidence of bone marrow toxicity, which could be marked by dropping hematocrit (Hct), WBC, or platelets levels. However, no significant drop in Hct, WBC, or platelets was observed indicating a lack of acute bone marrow toxicity.

Liver enzymes (Figure 6b) showed no significant elevation of aspartate transaminase (AST), alanine aminotransferase (ALT), alkaline phosphatase (ALP), or gamma-glutamyl transpeptidase (GGT). In addition, there was no elevation of albumin or total bilirubin levels, indicating normal liver function and absence of acute hepatoxicity. Review of blood chemistries reveals maintenance of electrolyte balance throughout IOSPM NP injection (Supporting Information, Supporting Information Figure 7). MR biodistribution data show that renal NP clearance is delayed in the macaque, and there is no elevated creatinine (Cr) or abnormal blood urea nitrogen (BUN)/Cr ratio that would suggest kidney dysfunction. These results confirm that IOSPM NPs have no acute toxicity to bone marrow or liver and display no apparent immunogenicity, which overcomes a major barrier for its clinical translation as a contrast agent.

CONCLUSIONS

Recognizing and understanding inter-species differences is critical for future translational studies to assess organ targeting and toxicity. One of the hurdles that usually delays translation from benchtop to clinical practice of nanomedicine is that we are not sure whether a given nanoparticle that works well in small animal models will still work the same in humans. This is mainly because the animal experiments were usually focused on one species and lack systematic comparisons between cross-species. Here we used noninvasive MRI to track IOSPM NPs through several important organs *in vivo* to investigate the biokinetics of nanoparticles in both mice and macaques. We used IOSPM NPs due to its great potential as a next generation clinical contrast agent that provides functionality to facilitate cancer therapeutic applications. Several iron oxide NPs (IOP) including Feridex, Combidex, and Ferumoxytol have been approved by the FDA as contrast agents and iron replacement therapy for clinical uses a decade ago.[32–33] However, their widespread use is limited due to issues with their stability and lot-to-lot variability as a result of the sensitivity of their physicochemical characteristics to manufacturing conditions.[33–34] These first generation IOPs had simple, physically absorbed coatings that lacked functionality. By contrast, IOSPM NPs developed in our lab have long-term colloidal stability and consistent physicochemical properties due to the presence of a highly dense and stable PEG coating.[22] Furthermore, IOSPM NPs have simple and well-defined composition, and both PEG and iron oxide are commonly used in humans as a component of drug formulations and contrast agents, respectively. The dense PEG coating and functional amine groups allow for further modifications of the base IOSPM NPs for specific targeting of cancer and delivery of therapeutics.[35]

We used 14 T MRI to acquire MR images of mice and 3T MRI to obtain MR images of macaques. Different field strengths were used because mouse anatomical structures are an order of magnitude smaller than those of the macaque (Figure 2b and Figure 3a) and imaging at a high spatial resolution of MRI allowed us to average over a similar number of voxels in the mouse and macaque (Supporting Information, Supporting Information Table

1), resulting in a good comparison of cross-species NP biokinetics. We took several approaches to improve MRI quantitation including special animal setting, control of respiratory gating, rational MRI sequences, applying T2*-W or QT2 imaging to different tissues based on their physiology, placement of ROIs to avoid large vessels, and choosing external jugular vein for vascular ROI to avoid aortic pulsatility of larger vascular structures. We were able to detect the subtle signal change (6%) in the brain with high contrast-to-noise using interleaved T2*-W imaging (Figures 2 and 3, Supporting Information Figure 5), a much more sensitive technique than conventional MRI QT2 imaging which typically has a lower limit of detectable signal change around 10–20%.

The biokinetics of IOSPM NPs in mice and macaques is similar in the blood, liver, spleen, and muscle. QT2 and T2*-W data from blood demonstrated zero-order elimination kinetics, with near-complete return to baseline within 4 h. The IOSPM NP profile in blood by MRI are consistent with macaque plasma iron measurement (Figure 5c) and mouse blood fluorescence measurement (Figure 5d). Our data suggest that *in vivo* T2 measurement of blood can function as a surrogate for relative plasma NP content in cases where invasive blood sampling is undesirable. In liver and spleen, T2 changes rapidly and saturates for the duration of imaging, suggesting increased NP uptake by the liver and spleen and NPs remain in the liver and spleen at 4 h. NPs entered liver and spleen primarily by sinusoidal vasculatures lined by macrophages.[36–37] The similar uptake by liver and spleen cross species might be due to the similar density of vasculatures across the species and low uptake of IOSPM NPs by macrophages. Our previous study showed that the highly dense and strongly bounded PEG coating resulted in low non-specific protein adsorption on NPs and a low uptake of NPs by macrophages.[22] Macrophages in liver in mice and NHPs are reported to be different.[38] Other studies show that iron oxide NPs degrades over time and disappears in approximately three weeks in liver.[17,39] Within the liver, opsonization by macrophages followed by degradation within acidic endosomes is the primary mechanism for NP degradation.[40] Studies show that no apparent difference in main enzymes in liver that play a critical role in the metabolism and pharmacokinetics of xenobiotics among species including man.[41] Both mice and monkeys showed little T2 change in muscle after NP injection, suggesting a negligible amount of NPs present in muscle.

The biokinetics of IOSPM NPs in mice and macaques is different in kidneys, brain, and bone marrow. The kidney was revealed to be the compartment with the greatest inter-species difference in biokinetics (Figure 5b). Compared to the other plots of Figure 5b, the nanoparticle kinetics of the kidney is much more divergent between the species than the other organs of interest. It is necessary to emphasize that our method does not specify relative amounts of renal excretion in either species. Obtaining such information would be possible through bladder catheterization and/or radiotracer monitoring. However, our data provides relative temporal trends in renal uptake and washout, during the time that NPs persist in blood. Prior work has suggested that careful attention to renal clearance is necessary, to avoid unexpected renal toxicity in human NP applications.[42] MR signal change within the renal pelvis indicates that renal clearance of IOPSM NPs occurs with a greater time delay in the primate compared to the mouse. The observed differences in renal clearance may be explained by species-dependent variations in glomerular filtration rates (GFR).[43] GFR in general, is inversely correlated with body mass or body surface area,[44]

suggesting that the IOSPM NP renal clearance delay observed in the macaque may be amplified in humans. These results confirm that utmost caution must be taken when making predictions regarding elimination of NPs by the human kidney.

Bone marrow displayed dissimilar washout kinetics with macaque exhibiting delayed washout of IOSPM NPs as compared to mice (Figure 5b). Marrow is a region of great clinical interest, as prolonged retention can have both positive implications for treatment studies of hematological malignancy, and negative implications for off-target bone marrow toxicity during the treatment of other organ systems. NHPs are relatively rich in lymphocytes while nude athymic mice lack mature T cells, however, it is unlikely the washout difference is due to an immune response since it would be expected that the reaction would take place faster in the monkeys containing intact T cells.[45] Researchers have previously showed that macrophages play a key role in observed species-dependent differences in bone marrow uptake of liposomal NPs[46] and may explain similar differences observed with IOSPM NP washout; however, further studies are needed to elucidate the role of macrophages in NP bone marrow uptake and washout.

It is known that iron oxide NPs are capable of passively crossing the intact blood-brain barrier (BBB) in small quantities, with the extent of crossing often augmented intentionally through active mechanisms such as the use of homing ligands.[47] Here, we observed brain uptake of IOSPM NPs for both mice and NHP, with washout delayed in the NHP. Complete return of blood T2 signal to baseline within 4 h eliminates blood partial volume effects as a possible explanation for these findings, confirming actual retention of NP within the brain of the macaque. The delayed washout from the macaque brain is likely due to nanoparticle-induced endothelial leakiness[48] and effects from species-dependent differences in cerebral spinal fluid (CSF) turnover rate.[49] Normalized expression of many membrane proteins that are determinant of endothelial permeability at the BBB are greater in mice than monkeys and could be partially responsible for the observed washout differences.[50] In addition, species differ not only at the expression level of transporter proteins but also in functional activity and more research is needed to understand the implications of these differences on NP uptake and washout in the brain. Turnover rates of CSF is species-dependent with mice and rats exhibiting far greater turnover rates than larger animals such as dogs, NHPs and, humans.[51] This species difference could play a major role in uptake and washout of hydrophilic compounds such as IOSPM NPs as high CSF flow rates may minimize diffusion of these hydrophilic particles into target tissue.[49]

In summary, we have systematically investigated PEGylated iron oxide NP biokinetics in macaques for the largest number of organ systems accomplished to date and have compared the biokinetics between macaques and mice. We found that blood T2 measurement can serve as a reliable surrogate for blood sampling. We conclude that NP biokinetics in primates and mice are similar in the majority of compartments including blood, liver, spleen, and muscle but differ in kidneys, marrow, and brain for our NP formulation. Our findings will provide researchers important information on whether NP biokinetics in NHPs is necessary in preclinical tests of similar NPs based on the targeted application of specific organs, which can significantly reduce costs for preclinical testing. Further, our study demonstrated that full-body MRI is practical, rapid, and cost-effective for tracking NPs non-invasively in

macaques with high temporal and spatial resolutions. The approach we developed here may be further used as a platform for testing other nanomaterial formulations and provide interesting springboards to understand important interspecies distinctions.

MATERIALS AND METHODS

Materials

All chemicals were purchased from Sigma-Aldrich (St. Louis, MO, USA) unless otherwise specified. 3-(triethoxysilyl)propyl succinic anhydride (SATES) was purchased from Gelest (Arlington, VA, USA). 2000 MW mono-amine functionalized poly(ethylene) glycol (mPEG2K-NH$_2$) was purchased from Laysan Bio (Arab, AL, USA).

NP synthesis and coating

50 mg of IOOA was suspended in 43 ml of anhydrous toluene followed by addition of 50 μl of triethylamine in a 3-neck round-bottom flask fitted with a Graham condenser. The flask was sealed with rubber septa and purged with nitrogen. The solution was heated to 100°C and 0.10 ml of SATES was added to the flask. 187.5 mg of mPEG2K-NH$_2$ was dissolved in 7 ml of anhydrous toluene and the resultant solution was added to the flask 15 min after the addition of SATES. An additional 50 μl of SATES was injected 1h after the mPEG2K-NH$_2$ injection, and the solution was reacted for a further 6 h and 45 minutes. The solution was transferred to a single-neck round-bottom flask and NPs were precipitated with hexane. The NP precipitate was dispersed in tetrahydrofuran (THF), sonicated for 10 min, and precipitated with hexane. The resulting NP pellet was suspended in 10 ml anhydrous THF and sonicated for 10 min. 62.5 mg of mPEG2K-NH$_2$ and 187.5 mg of 2000 MW bis(amine) functionalized PEG (PEG2K-bis(amine)) was dissolved in 12 ml of anhydrous THF and added to the NP solution. The flask was then sealed with a septum and purged with nitrogen. 12.5 mg of N,N^1-dicyclohexylcarbodiimide (DCC) was dissolved in 2 ml of anhydrous THF and added to the flask, and the reaction solution was placed in a sonication bath at 25°C and allowed to react for 16 h. Fully PEGylated NPs were precipitated with hexane, redispersed in 20 ml ethanol, sonicated for 10 min, and precipitated again with hexane. The pellet was fully dried and dispersed in PBS with sonication for 10 min.

NP size and zeta potential characterization

The initial hydrodynamic size of NPs was analyzed at 100 μg/ml in PBS (pH 7.4). NP stability in biological fluid was analyzed at 100 μg/ml in DMEM supplemented with 10% FBS and 1% antibiotic-antimycotic. The zeta potential of NPs was analyzed at 100 μg/ml in 20 mM HEPES buffer (pH 7.4).

TEM analysis of NPs

Samples were prepared by diluting NPs to 100 μg/ml in deionized H$_2$O and 5 μl of the dilute solution was placed on a formvar/carbon coated 300 mesh copper grid (Ted Pella, INC., Redding, CA). After 5 minutes, the NP solution was removed and the grid was allowed to dry overnight before imaging.

Cy5.5 labeling

IOSPM NPs (2 mg) were reacted with 0.5 mg of Cy5.5 (GE Healthcare, Piscataway, NJ, USA) in 100 mM sodium bicarbonate buffer, pH 8.5 for 1 h at room temperature, protected from light and with gentle rocking. The resultant IOSPM-Cy5.5 NPs were purified using size exclusion chromatography in S-200 resin equilibrated with PBS, and stored at 4oC. UV-vis spectrophotometric analysis was performed for Cy5.5-labeled samples. Data used for display (Figure 1h) were blanked against PBS. The system was then blanked with NPs in PBS and absorbance (673 nm) was determined for IOSPM-Cy5.5 NPs at an equivalent Fe concentration. Using an extinction coefficient of 2.09×10^5 $M^{-1}cm^{-1}$ and an NP molecular weight of 2×10^6 g/mol, the number of fluorophore/NP was determined to be 50. PBS solvent from Cy5.5-labeled samples was extracted by centrifugation in a 30 K MW cutoff spin column, with UV-vis testing performed on this sample to confirm lack of a Cy5.5 peak.

Nanoparticle administration

Sterile prepared IOSPM NPs were transferred into medical-grade saline (pH = 7.5), and injected at a dose of 2.4 mg Fe/kg for both mouse (nude athymic) and macaque (*macaca nemestrina*). NPs were administered in mice by tail vein injection over 5 s, and in macaques by saphenous vein injection over 5 min. All procedures were performed in accordance with University of Washington Institutional Animal Care and Use Committee regulations. Injected IOSPM NP volume was ~18 ml in macaque experiments, and ~120 μl in mouse experiments, with individual injection volumes adjusted for exact animal weight. Three macaques were approved for MRI scanning on the current protocol. Four macaques were approved for clinical laboratory evaluation of blood counts, blood chemistry, and liver enzymes. Six mice were utilized for MRI experiments, and 12 mice were used for a confirmatory fluorescence-based study of IOSPM-Cy5.5 NP biodistribution over the 4 h after injection. In this confirmatory mouse experiment, 200 μl of blood and whole extracted organs were harvested pre- and post-injection, and examined using NIRF imaging (IVIS Lumina II system, PerkinElmer).

In vivo mouse MRI

Mice were scanned with a Bruker 14 T vertical-bore imaging system (Ultrashield 600 WB Plus). 3 mice were positioned in a 25-mm single-channel ^{1}H radiofrequency (RF) receiving coil (PB Micro 2.5) centered on the abdominal region, and 3 separate mice were positioned with the head and neck at isocenter. Use of these two scanning groups was necessary for imaging of the head and full torso, given the limitations in coil length (longitudinal FOV ~6 cm). Head/neck imaging included a structural rapid acquisition with refocused echoes (RARE) sequence (TR/TE = 4000/27 ms, in-plane resolution 52×78 μm^2, matrix 384×256), T2*-weighted (T2*-W) 2-D fast low-angled shot (FLASH) (TR/TE = 1000/6 ms, in-plane resolution 98 μm^2, matrix 256×256), and quantitative T2 (QT2) multi-spin multi echo (MSME) (TR = 4000 ms, TE= 6.7 + 6n ms, [n = 0–16], in-plane resolution 52×78 μm^2, matrix 384×256). Abdominal scans maintained the same slice thickness, but were prescribed with larger FOV, used respiratory gating, and the following different parameters: structural RARE sequence (TR/TE = 691/5.5 ms, in-plane resolution 65×97 μm^2, matrix 384×256), T2*-W sequence (in-plane resolution 98 μm^2, matrix 256×256), QT2 sequence

(in-plane resolution 97×195 μm^2, matrix 256×128). Total image time for each sequence was approximately 4 min. Slices for sequential scans on a single mouse were prescribed identically, with 0.5 mm slice thickness. For head/neck scans, 14 coronal slices were positioned from the olfactory bulb extending to the cerebellum. For abdominal scans, 20 slices were positioned in the transverse plane with 0.75 mm interslice gap allowing coverage from the liver to the pelvic floor.

In vivo macaque MRI

Macaques were scanned with a Phillips 3 T Achieva MRI. All scans were obtained with respiratory gating. Baseline structural T2-W 3-D turbo spin echo images (TR/TE = 2500/250 ms, resolution 1 mm^3, matrix 452×226), QT2 2-D turbo spin echo images (TR/TE = $5000/12 + 12n$ [n = 0–8], in-plane resolution 0.94 mm^2, matrix 228×113, slice thickness 4 mm), and 3-D quantitative T2* (3-D fast field echo sequence, TR/TE = $75/6.9 + 6.9n$ [n = 0–8], resolution $0.94 \times 0.94 \times 4$ mm^3, matrix $228 \times 228 \times 113$) were obtained in coronal orientation over a body region spanning from the top of the head to the pelvis. 3-D T2*-W images were obtained of the head only, in an oblique plane (TR/TE = 45/25 ms, resolution $0.89 \times 0.89 \times 4$ mm^3, matrix 100×100). Interleaved scanning of brain (T2*-W) and head/torso (QT2) was performed after nanoparticle administration. Scan times were 6.2 min (T2W structural image) 20.3 min (QT2 image) 1.9 min (T2*-W image).

Magnetic characterization of aqueous nanoparticle samples

NP phantoms were constructed, *via* dilution of concentrated IOSPM NP stock to concentrations of 0 μg/ml, 10 μg/ml, 50 μg/ml, 100 μg/ml, 150 μg/ml, and 200 μg/ml in PBS. Tubes containing NPs were 2 mm in diameter for 14 T phantoms, and 1 cm in diameter for 3 T phantoms. Sample tubes containing NPs were fixated and surrounded by a homogeneous external PBS medium to minimize magnetic susceptibility fluctuations around the samples. Imaging of phantoms was performed using the same QT2 and T2*-W sequences used for *in vivo* imaging. T2 values, as well as T2*-W signal changes induced by NPs at each concentration were determined within circular 50-voxel ROIs at either field strength.

MRI Data Analysis

Analysis of MRI data was performed using FMRIB software library (FSL),[52] Bruker Paravision 5.1 analytic package, Phillips integrated software, Osirix (Pixmeo), and Matlab (Mathworks). Processing stages for QT2 and QT2* data included (i) ROI definition, (ii) automated T2 value calculation within the ROI (Paravision 5.1 or Phillips software), (iii) manual T2 calculation within the ROI by exponential least-squares fitting of the raw spin echo data (Matlab), and (iv) translation of the ROI over all images in the 4-D time-series, using anatomical landmarks to confirm appropriate ROI placement. Imaging of the head/neck in both macaque and mouse permitted automated rigid body registration/motion correction prior to the four analysis steps above (FSL, 3 degrees-of-freedom). Due to peristaltic movement within the abdomen and the non-cylindrical image contour, image registration could not be used reliably on body images.

Analysis of non-quantitative T2*-W data involved normalization of intensity within each image by signal amplitude of the adjacent water phantom to correct for temporal fluctuations

Author Manuscript

in hardware sensitivity and scan-to-scan differences in the pulse power/receiver gain settings. ROIs were defined and interrogated in an equivalent manner to QT2 and QT2* scans.

Further details regarding the NP PEGylation process, Cy5.5 conjugation, NIRF whole-organ imaging, MRI sequence parameters, and specific MR analytic methods are included in Supporting Information.

Whole-organ fluorescence measurement

NIRF imaging was performed on an IVIS Lumina II system (PerkinElmer, Waltham, Massachusetts). A total of 12 nude mice were used for the confirmatory biodistribution experiment. Cy5.5-labeled NPs were administered by lateral tail vein injections into 9 mice, with groups of 3 mice sacrificed at 1 h, 2 h, and 3.5 h. 3 additional mice were used as non-injected baseline fluorescence controls. Immediately after sacrifice, 200 μl blood samples were obtained from each mouse, and organs were harvested. NIRF images were acquired on an IVIS system, with excitation and emission filters for Cy5.5. Fluorescence data were analyzed using oval ROIs placed around the external border of each organ. Whole organ photon counts were averaged over the 3 animals in each of 4 groups.

Supplementary Material

Refer to Web version on PubMed Central for supplementary material.

Acknowledgments

References

1. Koo YEL, Reddy GR, Bhojani M, Schneider R, Philbert MA, Rehemtulla A, Ross BD, Kopelman R. Brain Cancer Diagnosis and Therapy with Nanoplatforms. Adv Drug Deliv Rev. 2006; 58:1556–1577. [PubMed: 17107738]

2. Ruggeri BA, Camp F, Miknyoczki S. Animal Models of Disease: Pre-Clinical Animal Models of Cancer and Their Applications and Utility in Drug Discovery. Biochem Pharmacol. 2014; 87:150–161. [PubMed: 23817077]

3. Jain RK, Stylianopoulos T. Delivering Nanomedicine to Solid Tumors. Nat Rev Clin Oncol. 2010; 7:653–664. [PubMed: 20838415]

4. Davis ME, Chen Z, Shin DM. Nanoparticle Therapeutics: An Emerging Treatment Modality for Cancer. Nat Rev Drug Discov. 2008; 7:771–782. [PubMed: 18758474]

5. Kroll A, Pillukat MH, Hahn D, Schnekenburger J. Current *in Vitro* Methods in Nanoparticle Risk Assessment: Limitations and Challenges. Eur J Pharm Biopharm. 2009; 72:370–377. [PubMed: 18775492]

6. Singh N, Jenkins GJ, Asadi R, Doak SH. Potential Toxicity of Superparamagnetic Iron Oxide Nanoparticles (SPION). Nano Rev. 2010; 1:1–15.

7. Arora S, Rajwade JM, Paknikar KM. Nanotoxicology and *in Vitro* Studies: The Need of the Hour. Toxicol Appl Pharmacol. 2012; 258:151–165. [PubMed: 22178382]

8. Singh M, Murriel CL, Johnson L. Genetically Engineered Mouse Models: Closing the Gap between Preclinical Data and Trial Outcomes. Cancer Res. 2012; 72:2695–2700. [PubMed: 22593194]

9. Khandhar AP, Ferguson RM, Arami H, Krishnan KM. Monodisperse Magnetite Nanoparticle Tracers for *in Vivo* Magnetic Particle Imaging. Biomaterials. 2013; 34:3837–3845. [PubMed: 23434348]

10. Faure AC, Dufort S, Josserand V, Perriat P, Coll JL, Roux S, Tillement O. Control of the *in Vivo* Biodistribution of Hybrid Nanoparticles with Different Poly(Ethylene Glycol) Coatings. Small. 2009; 5:2565–2575. [PubMed: 19768700]

11. Jain TK, Reddy MK, Morales MA, Leslie-Pelecky DL, Labhasetwar V. Biodistribution, Clearance, and Biocompatibility of Iron Oxide Magnetic Nanoparticles in Rats. Mol Pharm. 2008; 5:316–327. [PubMed: 18217714]

12. Al Faraj A, Lacroix G, Alsaid H, Elgrabi D, Stupar V, Robidel F, Gaillard S, Canet-Soulas E, Cremillieux Y. Longitudinal ^{3}He and Proton Imaging of Magnetite Biodistribution in a Rat Model of Instilled Nanoparticles. Magn Reson Med. 2008; 59:1298–1303. [PubMed: 18506795]

13. Dassler K, Roohi F, Lohrke J, Ide A, Remmele S, Hutter J, Pietsch H, Pison U, Schutz G. Current Limitations of Molecular Magnetic Resonance Imaging for Tumors As Evaluated with High-Relaxivity Cd105-Specific Iron Oxide Nanoparticles. Invest Radiol. 2012; 47:383–391. [PubMed: 22659596]

14. Lee PW, Hsu SH, Wang JJ, Tsai JS, Lin KJ, Wey SP, Chen FR, Lai CH, Yen TC, Sung HW. The Characteristics, Biodistribution, Magnetic Resonance Imaging and Biodegradability of Superparamagnetic Core-Shell Nanoparticles. Biomaterials. 2010; 31:1316–1324. [PubMed: 19959224]

15. Hoffman D, Sun M, Yang L, McDonagh PR, Corwin F, Sundaresan G, Wang L, Vijayaragavan V, Thadigiri C, Lamichhane N, Zweit J. Intrinsically Radiolabelled [^{59}Fe]-SPIONs for Dual Mri/Radionuclide Detection. Am J Nucl Med Mol Imaging. 2014; 4:548–560. [PubMed: 25250204]

16. Crayton SH, Elias DR, Al Zaki A, Cheng Z, Tsourkas A. ICP-MS Analysis of Lanthanide-Doped Nanoparticles As a Non-Radiative, Multiplex Approach to Quantify Biodistribution and Blood Clearance. Biomaterials. 2012; 33:1509–1519. [PubMed: 22100983]

17. Ruiz A, Hernandez Y, Cabal C, Gonzalez E, Veintemillas-Verdaguer S, Martinez E, Morales MP. Biodistribution and Pharmacokinetics of Uniform Magnetite Nanoparticles Chemically Modified with Polyethylene Glycol. Nanoscale. 2013; 5:11400–11408. [PubMed: 23832394]

18. Schlachter EK, Widmer HR, Bregy A, Lonnfors-Weitzel T, Vajtai I, Corazza N, Bernau VJ, Weitzel T, Mordasini P, Slotboom J, Herrmann G, Bogni S, Hofmann H, Frenz M, Reinert M. Metabolic Pathway and Distribution of Superparamagnetic Iron Oxide Nanoparticles: *in Vivo* Study. Int J Nanomedicine. 2011; 6:1793–1800. [PubMed: 21980242]

19. Al Faraj A, Cieslar K, Lacroix G, Gaillard S, Canet-Soulas E, Cremillieux Y. *In Vivo* Imaging of Carbon Nanotube Biodistribution Using Magnetic Resonance Imaging. Nano Lett. 2009; 9:1023–1027. [PubMed: 19199447]

20. Barrefelt A, Saghafian M, Kuiper R, Ye F, Egri G, Klickermann M, Brismar TB, Aspelin P, Muhammed M, Dahne L, Hassan M. Biodistribution, Kinetics, and Biological Fate of SPION Microbubbles in the Rat. Int J Nanomedicine. 2013; 8:3241–3254. [PubMed: 24023513]

21. Herodin F, Thullier P, Garin D, Drouet M. Nonhuman Primates Are Relevant Models for Research in Hematology, Immunology and Virology. Eur Cytokine Netw. 2005; 16:104–116. [PubMed: 15941681]

22. Fang C, Bhattarai N, Sun C, Zhang M. Functionalized Nanoparticles with Long-Term Stability in Biological Media. Small. 2009; 5:1637–1641. [PubMed: 19334014]

23. Park J, An K, Hwang Y, Park JG, Noh HJ, Kim JY, Park JH, Hwang NM, Hyeon T. Ultra-Large-Scale Syntheses of Monodisperse Nanocrystals. Nat Mater. 2004; 3:891–895. [PubMed: 15568032]

24. Prantner AM, Scholler N. Biological Barriers and Current Strategies for Modifying Nanoparticle Bioavailability. J Nanosci Nanotechnol. 2014; 14:115–125. [PubMed: 24730254]

25. Jun YW, Huh YM, Choi JS, Lee JH, Song HT, Kim S, Yoon S, Kim KS, Shin JS, Suh JS, Cheon J. Nanoscale Size Effect of Magnetic Nanocrystals and Their Utilization for Cancer Diagnosis *via* Magnetic Resonance Imaging. J Am Chem Soc. 2005; 127:5732–5733. [PubMed: 15839639]

26. Longmire M, Choyke PL, Kobayashi H. Clearance Properties of Nano-Sized Particles and Molecules As Imaging Agents: Considerations and Caveats. Nanomedicine. 2008; 3:703–717. [PubMed: 18817471]

27. Bowen CV, Zhang X, Saab G, Gareau PJ, Rutt BK. Application of the Static Dephasing Regime Theory to Superparamagnetic Iron-Oxide Loaded Cells. Magn Reson Med. 2002; 48:52–61. [PubMed: 12111931]

28. Yablonskiy DA, Haacke EM. Theory of NMR Signal Behavior in Magnetically Inhomogeneous Tissues: The Static Dephasing Regime. Magn Reson Med. 1994; 32:749–763. [PubMed: 7869897]

29. Simon GH, Bauer J, Saborovski O, Fu Y, Corot C, Wendland MF, Daldrup-Link HE. T1 and T2 Relaxivity of Intracellular and Extracellular USPIO at 1.5t and 3t Clinical Mr Scanning. Eur Radiol. 2006; 16:738–745. [PubMed: 16308692]

30. Sun C, Du K, Fang C, Bhattarai N, Veiseh O, Kievit F, Stephen Z, Lee D, Ellenbogen RG, Ratner B, Zhang M. PEG-Mediated Synthesis of Highly Dispersive Multifunctional Superparamagnetic Nanoparticles: Their Physicochemical Properties and Function *in Vivo*. ACS Nano. 2010; 4:2402–2410. [PubMed: 20232826]

31. Lee MJ, Veiseh O, Bhattarai N, Sun C, Hansen SJ, Ditzler S, Knoblaugh S, Lee D, Ellenbogen R, Zhang M, Olson JM. Rapid Pharmacokinetic and Biodistribution Studies Using Cholorotoxin-Conjugated Iron Oxide Nanoparticles: A Novel Non-Radioactive Method. PLoS One. 2010; 5:e9536. [PubMed: 20209054]

32. Lee N, Hyeon T. Designed Synthesis of Uniformly Sized Iron Oxide Nanoparticles for Efficient Magnetic Resonance Imaging Contrast Agents. Chem Soc Rev. 2012; 41:2575–2589. [PubMed: 22138852]

33. Hope MD, Hope TA, Zhu C, Faraji F, Haraldsson H, Ordovas KG, Saloner D. Vascular Imaging with Ferumoxytol As a Contrast Agent. Am J Roentgenol. 2015; 205:W366–W373. [PubMed: 26102308]

34. Corot C, Robert P, Idee JM, Port M. Recent Advances in Iron Oxide Nanocrystal Technology for Medical Imaging. Adv Drug Deliv Rev. 2006; 58:1471–1504. [PubMed: 17116343]

35. Wang K, Kievit FM, Sham JG, Jeon M, Stephen ZR, Bakthavatsalam A, Park JO, Zhang M. Iron-Oxide-Based Nanovector for Tumor Targeted Sirna Delivery in an Orthotopic Hepatocellular Carcinoma Xenograft Mouse Model. Small. 2016; 12:477–487. [PubMed: 26641029]

36. Sun C, Lee JS, Zhang M. Magnetic Nanoparticles in MR Imaging and Drug Delivery. Adv Drug Deliv Rev. 2008; 60:1252–1265. [PubMed: 18558452]

37. Kievit FM, Zhang M. Cancer Nanotheranostics: Improving Imaging and Therapy by Targeted Delivery across Biological Barriers. Adv Mater. 2011; 23:H217–H247. [PubMed: 21842473]

38. Vaure C, Liu Y. A Comparative Review of Toll-Like Receptor 4 Expression and Functionality in Different Animal Species. Front Immunol. 2014; 5:316. [PubMed: 25071777]

39. Levy M, Luciani N, Alloyeau D, Elgrabli D, Deveaux V, Pechoux C, Chat S, Wang G, Vats N, Gendron F, Factor C, Lotersztajn S, Luciani A, Wilhelm C, Gazeau F. Long Term *in Vivo* Biotransformation of Iron Oxide Nanoparticles. Biomaterials. 2011; 32:3988–3999. [PubMed: 21392823]

40. Arami H, Khandhar A, Liggitt D, Krishnan KM. *In Vivo* Delivery, Pharmacokinetics, Biodistribution and Toxicity of Iron Oxide Nanoparticles. Chem Soc Rev. 2015; 44:8576–8607. [PubMed: 26390044]

41. Martignoni M, Groothuis GM, de Kanter R. Species Differences between Mouse, Rat, Dog, Monkey and Human Cyp-Mediated Drug Metabolism, Inhibition and Induction. Expert Opin Drug Metab Toxicol. 2006; 2:875–894. [PubMed: 17125407]

42. Soo Choi H, Liu W, Misra P, Tanaka E, Zimmer JP, Ipe BI, Bawendi MG, Frangioni JV. Renal Clearance of Quantum Dots. Nat Biotechnol. 2007; 25:1165–1170. [PubMed: 17891134]

43. Fleck C. Determination of the Glomerular Filtration Rate (GFR): Methodological Problems, Age-Dependence, Consequences of Various Surgical Interventions, and the Influence of Different Drugs and Toxic Substances. Physiol Res. 1999; 48:267–279. [PubMed: 10638678]

44. Donadio C, Lucchesi A, Tramonti G, Bianchi C. Creatinine Clearance Predicted from Body Cell Mass Is a Good Indicator of Renal Function. Kidney Int Suppl. 1997; 63:S166–S168. [PubMed: 9407449]

45. Martin RA, Brott DA, Zandee JC, McKeel MJ. Differential Analysis of Animal Bone Marrow by Flow Cytometry. Cytometry. 1992; 13:638–643. [PubMed: 1451595]

46. Sou K, Goins B, Oyajobi BO, Travi BL, Phillips WT. Bone Marrow-Targeted Liposomal Carriers. Expert Opin Drug Deliv. 2011; 8:317–328. [PubMed: 21275831]

47. Petros RA, DeSimone JM. Strategies in the Design of Nanoparticles for Therapeutic Applications. Nat Rev Drug Discov. 2010; 9:615–627. [PubMed: 20616808]

48. Setyawati MI, Tay CY, Leong DT. The Gap between Endothelial Cells: Key to the Quick Escape of Nanomaterials? Nanomedicine. 2014; 9:1591–1594. [PubMed: 25321168]

49. Deo AK, Theil FP, Nicolas JM. Confounding Parameters in Preclinical Assessment of Blood-Brain Barrier Permeation: An Overview with Emphasis on Species Differences and Effect of Disease States. Mol Pharm. 2013; 10:1581–1595. [PubMed: 23256608]

50. Ito K, Uchida Y, Ohtsuki S, Aizawa S, Kawakami H, Katsukura Y, Kamiie J, Terasaki T. Quantitative Membrane Protein Expression at the Blood-Brain Barrier of Adult and Younger Cynomolgus Monkeys. J Pharm Sci. 2011; 100:3939–3950. [PubMed: 21254069]

51. Lu Y, Barton HA, Leung L, Zhang L, Hajos-Korcsok E, Nolan CE, Liu J, Becker SL, Wood KM, Robshaw AE, Taylor CK, O'Neill BT, Brodney MA, Riddell D. Cerebrospinal Fluid B-Amyloid Turnover in the Mouse, Dog, Monkey and Human Evaluated by Systematic Quantitative Analyses. Neurodegener Dis. 2013; 12:36–50. [PubMed: 22922480]

52. Jenkinson M, Beckmann CF, Behrens TE, Woolrich MW, Smith SM. FSL. Neuroimage. 2012; 62:782–790. [PubMed: 21979382]
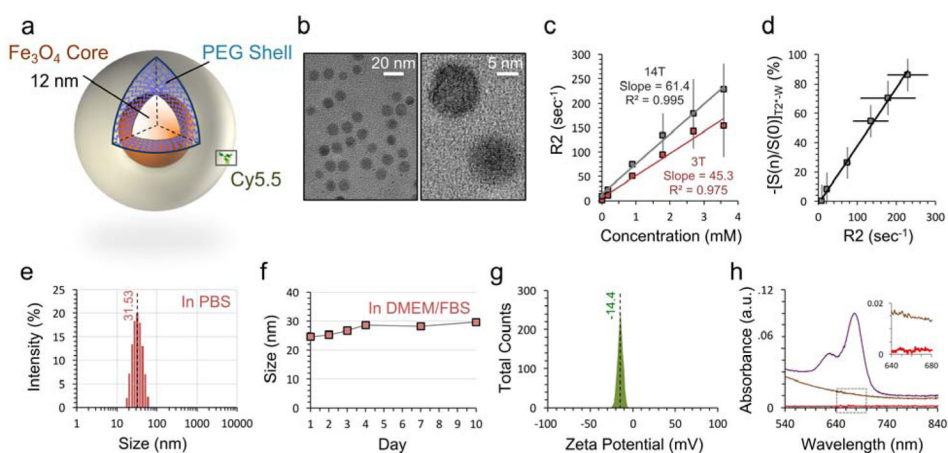
Figure 1. Characterization of iron oxide nanoparticles

a, Schematic of nanoparticle with metallic 12 nm iron oxide core and amine-terminated PEG shell. The core and shell are joined by a cross-linked siloxane intermediate layer. Cy5.5 fluorophore is conjugated on a subset of the nanoparticles. **b,** TEM of the nanoparticle at low magnification (left) demonstrates monodispersity and spherical core shape. High magnification (right) displays linear features of the iron oxide crystal lattice. **c,** Magnetic T2 relaxivity of IOSPM NPs in PBS at 25 °C is calculated to be 45.3 $s^{-1}mM^{-1}$ at 3 T (red), and 61.4 $s^{-1}mM^{-1}$ at 14 T (grey). **d,** Quantitative IOSPM NP data at 14 T. NP concentrations and R2 values in (**c**) are plotted against respective T2*-W signal changes from baseline, demonstrating a linear relationship between these two measurement techniques. **e,** Dynamic light scattering (DLS) data demonstrates an average NP hydrodynamic size of 31.53 nm in PBS, with good size uniformity. **f,** Monitoring of NP size in DMEM/FBS reveals <5 nm change over 10 days, with a stable hydrodynamic size of ~29 nm reached between days 4–10. **g,** Zeta-potential measurement shows a net-negative particle surface charge of −14.4 mV. **h,** Confirmatory biodistribution experiments in mice required fluorophore labeling with Cy5.5. UV-visible spectra for NP samples prior to Cy5.5 conjugation (brown) and after conjugation and purification (purple) confirm presence of the fluorophore (UV-vis baseline was PBS, and samples of equivalent Fe_3O_4 concentration are shown). The aqueous buffer from the purified Cy5.5-labeled sample was extracted by centrifugation (30 K MW cutoff spin column), to demonstrate good binding, from an absence of Cy5.5 in the supernatant (red, inset).
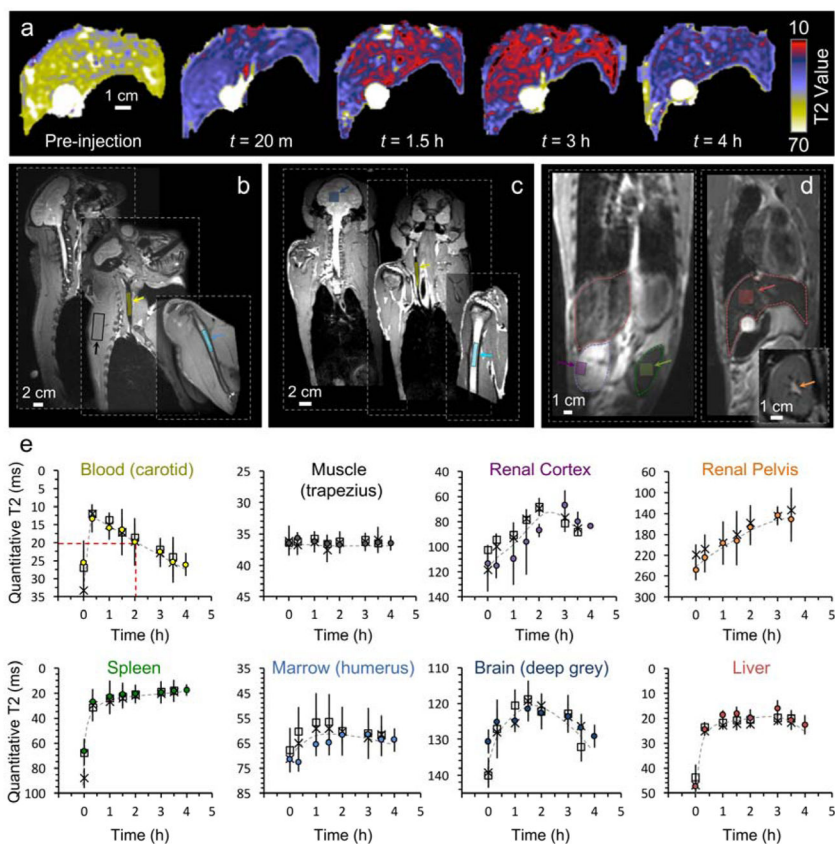
Figure 2. Non-invasive measurement of IOSPM NP biodistribution in macaques

a, Quantitative T2 maps of the macaque liver show homogeneous changes in T2 throughout the organ after IOSPM NP injection. **b,** Sagittal and **c,** coronal T2-weighted structural images of the head and upper torso are used to display ROIs for quantitative analysis of blood (yellow), muscle (grey), bone marrow (light blue), and deep grey matter of the brain (dark blue). **d,** Example raw images from the multi-spin-echo sequence demonstrate ROIs of the liver (red), spleen (green), and renal cortex (purple). A separate slice is used to display the renal pelvis (orange, inset). ROIs were chosen to avoid obvious large vessels within each compartment. **e,** Average T2 was calculated within ROIs for each time point collected over a 4-h period. Colored circles represent T2 values from the first macaque (matched to color of respective ROIs), adjacent open squares show data from the second macaque, and X symbols designate the third macaque. Dashed grey lines are a guide to the eye. Red dashed lines added to the blood compartment highlight the equivalent bloodstream kinetics in the three macaques. Each compartment displays a signature time course. Due to positioning of slices and anatomical differences between animals, a reliable ROI within the renal pelvis could only be obtained for the second macaque scanned.
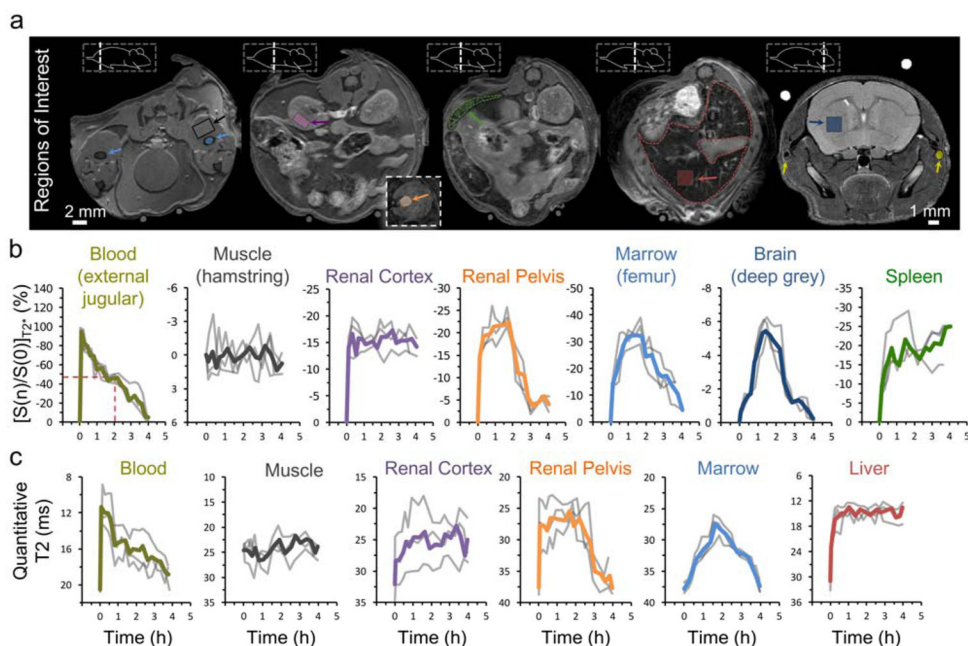
Figure 3. Non-invasive measurement of IOSPM NP biodistribution in mice

a, Transverse cross-sections display mouse anatomy from pelvis to head (slice position relative to the mouse shown in adjacent graphic). External jugular vein was used as the blood ROI (yellow) due to low vessel pulsatility and minimal respiratory artifact in the surrounding tissues. Hamstrings provided the largest area for muscle ROIs (black). Femur provided a consistent, cylindrical compartment for bone marrow (light blue). ROIs are also shown in the renal cortex (purple), renal pelvis (orange, inset), spleen (green), liver (red), and brain (dark blue). Dashed outlines indicate borders of the liver (red) and spleen (green). Water phantom can be seen below the abdomen and above the head, with differences in phantom brightness indicative of the shorter TE used in structural imaging of the abdomen. **b,** T2*-weighted signal change from pre-injection baseline (expressed as percent), after normalization of each value with corresponding signal produced by the water phantom. Excellent correspondence is seen over time in signal behavior between individual animals (grey). Average normalized signal change between animals is displayed as the colored line. T2*-W signal change after NP injection could not be reliably determined in the liver due to low T2*-W signal at baseline. **c,** Quantitative T2 imaging provides trends for the blood, muscle, renal cortex, and renal pelvis consistent with T2*-W data. Spin-echo refocusing allows visualization of signal change in the liver.
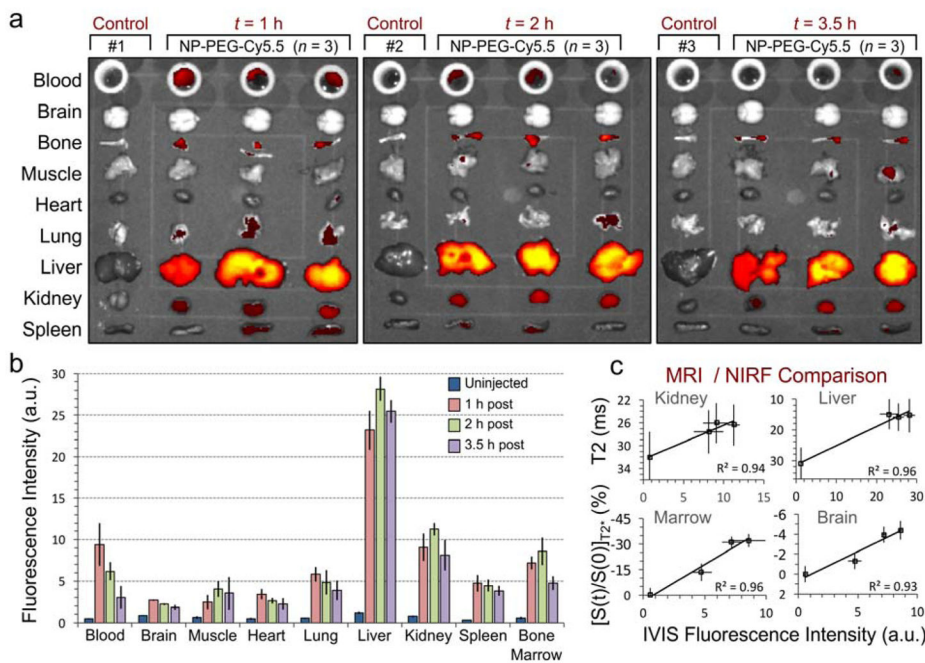
Figure 4. NIRF imaging of whole-organ NP uptake

a, 12 mice were used to confirm *in vivo* MRI patterns of IOSPM NP biodistribution with *ex vivo* organ fluorescence intensity measurement. Consecutive panels show blood (200 μl) and whole organs (brain, bone, muscle, heart, lung, liver, kidney, and spleen) from mice sacrificed at 1 h, 2 h, and 3.5 h. Organs at each experimental timepoint were imaged alongside organs from separate non-injected control mice. Images display highest IOSPM-Cy5.5 NP uptake in the liver, with visible fluorescence change in the blood, bone, lung, kidney, and spleen. **b,** Fluorescence intensity in all organs was calculated, and is displayed graphically for each time point. Error bars represent ± standard deviation of the mean from the three independent measurements. **c,** A direct comparison between MR and fluorescence results suggests a linear relationship between the two measurement techniques. Such linearity is demonstrated both for examples using QT2 imaging (displayed for the kidney and liver), and with T2*-W imaging (shown in the marrow and brain). R^2 values ranging from 0.93 to 0.96 are shown, adjacent to the respective linear fits.
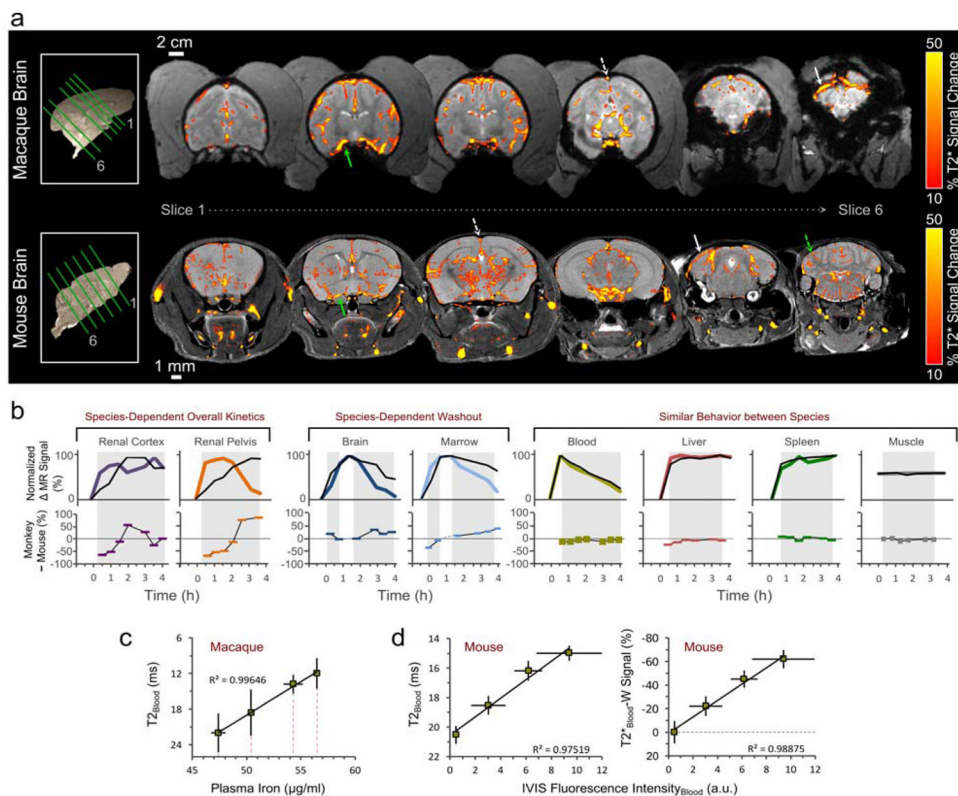
Figure 5. Inter-species comparison of IOSPM biodistribution

a, For both species, the largest intracranial NP signal change occurs in the vasculature. T2*-W signal is shown across 6 brain slices, 30 min after NP injection, for macaque (top row) and mouse (bottom row). A minimum threshold of 10% eliminates visible signal change from most regions other than the large vessels, which display localized signal changes up to 60%. NP highlights the deep cerebral draining veins in both species, and in the case of the mouse, generates small signal markings from radially oriented vessels in the cerebellum (dashed green arrow). Solid green arrow depicts middle cerebral artery, dashed white arrow points to superior sagittal sinus and solid white arrow points to transverse sinus. **b,** The relative kinetics of NP uptake and elimination are compared between mouse (colored line) and macaque (black line), by modifying the observed minimum and maximum signal changes to exist on a range from 0 to 100 %. Data from the mouse, which were obtained at higher temporal frequency, were sub-sampled using only points acquired at equivalent times to the macaque. The equivalently scaled data was then subtracted, with negative values signifying greater relative uptake in the mouse, and positive values signifying greater relative uptake in the macaque (bottom plots in **b**). Shadowed regions indicate data that were used in the comparison. Renal uptake and washout differ for the two species. Data from the brain and marrow are consistent with prolonged NP retention in the macaque compared to the mouse. Blood, liver, spleen, and muscle display similar biokinetics throughout the timeframe investigated. **c,** A linear relationship is seen ($R^2 = 0.996$) between macaque blood T2 values and directly measured ICP iron content of blood plasma samples. **d,** A linear relationship is observed between mouse bloodstream T2 value and blood NIRF intensity ($R^2 = 0.975$, left
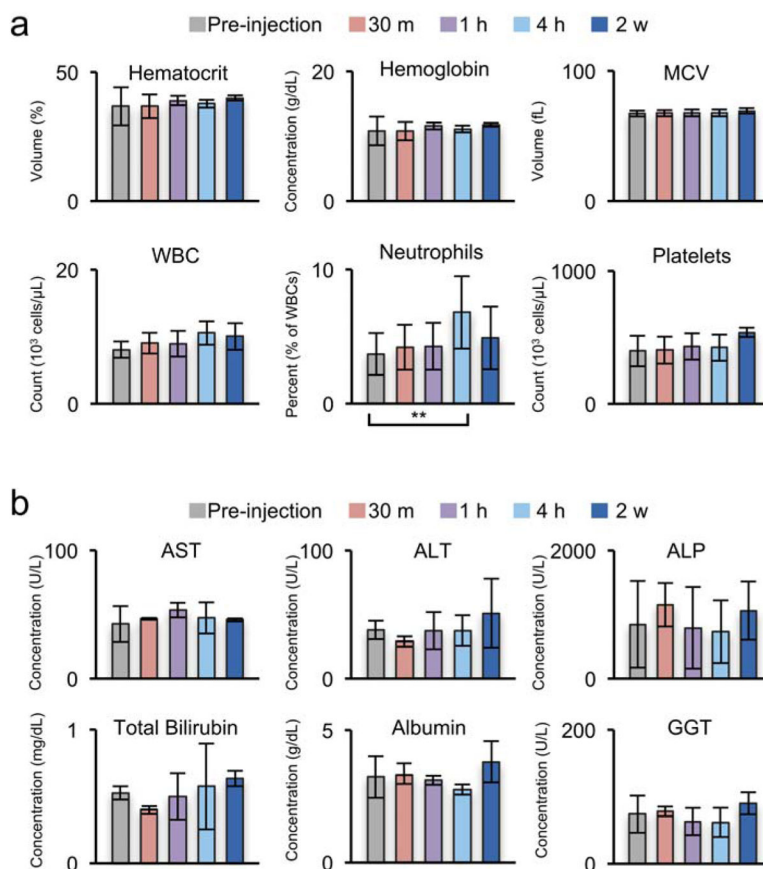
plot). Change in T2*-W signal displays a similarly linear relationship with NIRF blood fluorescence intensity ($R^2 = 0.989$, right plot).

Figure 6. Macaque laboratory values before and after IOSPM injection

a, Complete blood cell count, and **b,** liver enzymes are displayed for three macaques. A minimal increase in the percent of white blood account (WBC) corresponding to neutrophils (**$p < 0.05$) were observed 4 h post-injection; however, these values returned to normal by 2 weeks. WBC remained below laboratory criteria for abnormal elevation in the macaque (<14) (**a**). Liver enzymes showed no significant change over the course of the study (**b**). Averages and standard deviations were determined from blood samples of 4 macaques.